Catalysis Science & Technology

PAPER

View Article Online
View Journal | View Issue

Check for updates

Cite this: *Catal. Sci. Technol.*, 2019, **9**, 6606

N-doped hierarchical porous metal-free catalysts derived from covalent triazine frameworks for the efficient oxygen reduction reaction†

Yaqi Cao,[a] Yuanzhi Zhu,[b] Xifan Chen,[a] Bahreselam Sielu Abraha,[a]
Wenchao Peng,[a] Yang Li,[a] Guoliang Zhang,[a]
Fengbao Zhang[a] and Xiaobin Fan*[a]

Received 9th August 2019,
Accepted 17th October 2019

DOI: 10.1039/c9cy01597c

rsc.li/catalysis

The oxygen reduction reaction (ORR) is a core reaction in energy conversion and storage devices. Herein, nitrogen-doped hierarchical micro/mesoporous carbon ORR catalysts derived from covalent triazine frameworks (CTFs) were prepared based on a rational bottom-up strategy. Benefiting from its high specific surface area (1925 m^2 g^{-1}), hierarchical micro/mesoporous structure (0–12 nm), three-dimensional conductive network and high pyridinic N and graphitic N content, the optimal CTF-Super P-10 composite catalyst exhibits an onset potential of 0.981 V and a half-wave potential of 0.883 V, with a high limiting current density of around 5.31 mA cm^{-2} under alkaline conditions. It shows a dominant four-electron pathway, strong stability, and better methanol tolerance than commercial Pt/C in both alkaline conditions and acidic conditions, highlighting a promising strategy for designing high performance metal-free ORR catalysts.

Introduction

The oxygen reduction reaction (ORR) plays a key role in many sustainable energy storage and conversion systems, such as fuel cells and metal–air batteries.[1] However, the ORR process is subject to sluggish kinetics due to its complex multi-electron transfer steps.[2] Another major challenge is the high cost and scarcity of precious Pt metal, which has been regarded as the most efficient and common catalyst for the ORR.[3] Therefore, it is urgent to design low cost and earth-abundant catalysts with comparable electrocatalytic activity towards the ORR. Compared with metal-based catalysts, which usually suffer from dissolution and agglomeration during the ORR process,[4,5] the accessible and eco-friendly metal-free catalysts, especially carbon-based catalysts, have caught increasing attention.[6,7] Previous studies have shown that metal-free carbon-based catalysts that meet the following conditions tend to show excellent ORR performance: three-dimensional pore structure, good electrical conductivity and abundant active sites.[8–15]

Among lots of carbon-based candidates, the layered covalent triazine frameworks (CTFs), a new kind of N-rich covalent organic frameworks (COFs) linked together with 1,3,5-triazine units, have attracted particular interest.[16] CTFs show permanent porosity, strong thermal stability and precisely controllable structures like other COFs.[17] In particular, CTFs feature tunable nitrogen doping by selecting appropriate aromatic nitriles as monomers. The high N/C ratio of the building blocks is beneficial to the formation of C–N active sites, and it has been demonstrated that both pyridinic N and graphitic N species are effective in promoting the ORR.[18–22] Besides, attributed to the mixing of zinc chloride and nitrile monomers at the molecular scale, the CTFs generally show a highly developed microporous structure.[23,24] Despite the reports of some CTF-based ORR catalysts,[5,25–34] the electrical conductivity of CTF-based metal-free carbon materials is commonly unsatisfactory, which limits their electrochemical application. Developing a well-defined hierarchical micro/mesoporous structure derived from CTFs with excellent conductivity and small mass transport resistance remains a great challenge.

Herein, N-doped hierarchical porous carbon materials derived from CTFs were prepared by ionothermal synthesis and pyrolysis based on the bottom-up strategy.[9,26] To adjust the porous structure and form a three-dimensional conductive network, different ratios of spherical conductive carbon black (Super P) in the precursors were evaluated, and a high

---

[a] School of Chemical Engineering and Technology, State Key Laboratory of Chemical Engineering, Collaborative Innovation Center of Chemical Science and Engineering, Tianjin University, Tianjin 300350, China.
E-mail: xiaobinfan@tju.edu.cn

[b] Faculty of Chemical Engineering, Yunnan Provincial Key Laboratory of Energy Saving in Phosphorus Chemical Engineering and New Phosphorus Materials, The Higher Educational Key Laboratory for Phosphorus Chemical Engineering of Yunnan Province, Kunming University of Science and Technology, Kunming 650500, China

† Electronic supplementary information (ESI) available. See DOI: 10.1039/c9cy01597c

synthesis temperature (900 °C) was used to increase the mesoporosity and conductivity.[25] The results show that the addition of appropriate amounts of Super P can significantly increase the mesoporous part of the catalysts, enlarge the specific surface area and raise the content of pyridinic N and graphitic N. Specifically, CTF-Super P-10, synthesized from 1,4-dicyanobenzene, Super P, and zinc chloride at a molar ratio of 1 : 10 : 10, shows a hierarchical micro/mesoporous structure and excellent conductivity. Compared with most metal-free catalysts and commercial Pt/C, it exhibits superior ORR performance under both alkaline conditions and acidic conditions.

Experimental

Materials

1,4-Dicyanobenzene ($C_8H_4N_2$, 98%, Heowns), Super P, anhydrous zinc chloride ($ZnCl_2$, 98%, Tokyo Chemical Industry), Pt/C (Pt 20% mass loading on carbon black, Johnson Matthey), hydrochloric acid (HCl, 36.5%, Guangfu), THF [$(CH_2)_4O$, 99.9%, Yuanli], isopropyl alcohol (C_3H_8O, 99.9%, Yuanli) and Nafion (5%, Sigma Aldrich). All materials were used without further purification.

Synthesis of CTF-Super P catalysts

The CTF-Super P catalysts were synthesized by ionothermal synthesis and pyrolysis, partly according to the previous literature.[16,26] The 1,4-dicyanobenzene monomer, $ZnCl_2$, and Super P (molar ratio of 1 : 10 : 0 for CTF, 1 : 10 : 5 for CTF-Super P-5, 1 : 10 : 10 for CTF-Super P-10, 1 : 10 : 15 for CTF-Super P-15 and 0 : 10 : 10 for Super P) were transferred into a glass ampoule (3 × 15 cm) under an Ar atmosphere in a glove box. The ampoules were evacuated, sealed and heated (3 °C min^{-1} ramping) to 400 °C for 20 h. The ampoules were then cooled down to room temperature and opened. The products were subsequently ground into fine powders and heated (3 °C min^{-1} ramping) in an Ar atmosphere to 900 °C for 2 h, and then leached in 0.5 M HCl at 60 °C for 6 h. Afterwards, the samples were filtered and washed with deionized water and THF. Finally, the black powders were dried in a vacuum overnight at 60 °C.

Characterization

The catalysts were investigated by XRD (Bruker D8 FOCUS, CuK_α radiation) and Raman spectroscopy (NT-MDT with 633 nm laser excitation). The morphologies and distribution of elements were characterized by SEM (Hitachi, S-4800), TEM and EDS mapping (JEOL, JEM-2100F). N_2 adsorption/desorption measurements (BJBulider SSA-7000) were carried out for analyzing the specific surface area and pore volume. The mesoporous size distribution is determined by the Barrett–Joyner–Halenda (BJH) method from the desorption isotherms. Further composition and valence state information was obtained by XPS (Thermo Scientific, ESCALAB 250 XI).

Electrochemical measurements

Electrochemical characterization was carried out on a CHI760E electrochemical workstation using a three-electrode configuration, where the working electrode was a glassy carbon RDE or a RRDE (Pine Research Instrumentation) coated with catalysts, the reference electrode was an Ag/AgCl electrode (in 3.5 M KCl solution), and the counter electrode was a gauze Pt electrode. To rule out the possibility of the influence of the counter electrode on the electrochemical measurements, related ORR data were also investigated with a graphite rod electrode (a carbon counter electrode). The electrolyte was a 0.1 M KOH aqueous solution or a 0.1 M $HClO_4$ aqueous solution. The ink was prepared by ultrasonically dispersing 5.0 mg of each catalyst powder in 0.5 mL solution of a mixture of Nafion (5 wt%, 20 μL), isopropyl alcohol (290 μL), and distilled water (190 μL). Then, 15 μL of the prepared catalyst ink was pipetted onto a polished glassy carbon electrode surface (0.196 cm^2) and dried at room temperature. The loading amount of catalyst was determined to be 0.70 mg cm^{-2}. For comparison, commercial 20% Pt/C was prepared on the electrode using a similar procedure as described above with a Pt/C loading of 1.27 mg cm^{-2} (Pt loading is 0.25 mg cm^{-2}).

All potentials reported in this article were converted to the reversible hydrogen electrode (RHE) scale. ORR linear sweep voltammetry (LSV) measurements were performed on a rotating disc electrode (RDE) in O_2-saturated 0.1 M KOH solution or 0.1 M $HClO_4$ solution and carried out from 1.0 to 0.2 V *vs.* RHE with background subtraction at a scan rate of 10 mV s^{-1} and rotating speed of 1600 rpm. All background curves measured in N_2-saturated electrolytes were subtracted to eliminate capacitive currents. Based on the Koutecky–Levich (K–L) equations, the electron transfer number and kinetic current density were obtained: $1/J = 1/J_k + 1/J_d = 1/J_k + 1/(B\omega^{1/2})$, $B = 0.2nFC_0(D_0)^{2/3}v^{-1/6}$, where J_k is the kinetic current density (mA cm^{-2}), J_d is the limiting diffusion current density (mA cm^{-2}), J is the measured current density (mA cm^{-2}), n is the overall number of electrons transferred in oxygen reduction, F is the Faraday constant, C_0 is the bulk concentration of O_2, D_0 is the diffusion coefficient of O_2, and v is the kinetic viscosity of the electrolyte. For the RRDE measurement, the disk potential was scanned from 0.8 to 0.2 V *vs.* RHE at 10 mV s^{-1}, and the ring potential was set as 1.4 V *vs.* RHE. The H_2O_2 yield and electron transfer number (n) were calculated by: $H_2O_2 = 200 \times (I_r/N)/(I_d + I_r/N)$; $n = 4 \times I_d/(I_d + I_r/N)$, where I_d is the disk current (mA), I_r is the ring current (mA), and N is the current collection efficiency of the Pt ring (0.37).

Results and discussion

As shown in Scheme 1, a series of CTF-Super P catalysts were synthesized *via* a bottom-up technology. The aromatic nitriles were first polymerized into CTFs at 400 °C for 20 h. Molten $ZnCl_2$ was used as the solvent and catalyst, and mixed with CTF at the molecular level.[16] The polymerization of nitriles at 400 °C produces microporous polymers, and then heating at

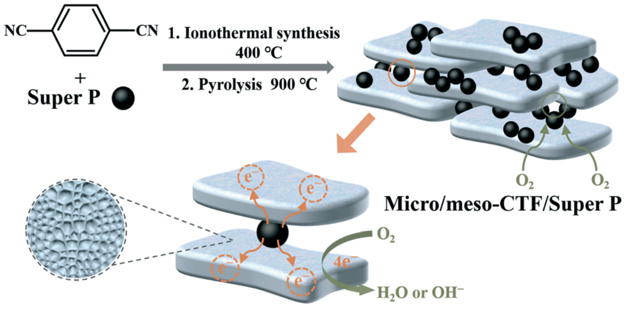

Scheme 1 The bottom-up construction of hierarchical micro/mesoporous CTF-Super P as metal-free ORR catalysts.

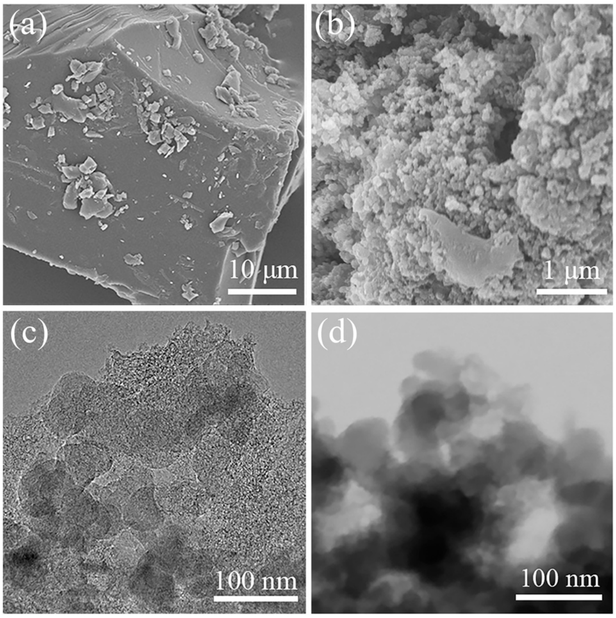

Fig. 2 SEM images of (a) CTF and (b) CTF-Super P-10; (c) TEM and (d) STEM images of CTF-Super P-10.

900 °C for 2 h produces the N-doped carbon catalysts,[25] followed by acid-leaching to remove the unreacted zinc salt. To increase the mesoporous portion and improve electrical conductivity, spherical conductive carbon black (Super P) was added to the precursors. Different ratios of the aromatic nitriles to Super P were chosen to tune the compositions and pore structures, and the ORR performance of the obtained catalysts was systematically evaluated (1,4-dicyanobenzene, zinc chloride, and Super P at a molar ratio of 1 : 10 : 0 for CTF, 1 : 10 : 5 for CTF-Super P-5, 1 : 10 : 10 for CTF-Super P-10 and 1 : 10 : 15 for CTF-Super P-15).

The X-ray diffraction (XRD) patterns of all the obtained samples have a broad peak at 2θ = 22–26° (Fig. 1a), which corresponds to amorphous carbon.[16] With the proportion of Super P increased, the width of the main peak at half maxima becomes smaller, and the peak shifts from 22.3° to 25.2°. This result can be explained by the increased contribution of Super P particles, which are carbon spheres with higher crystallinity. As shown in the Raman spectra (Fig. 1b), all samples display two prominent peaks at 1320 cm^{-1} and 1582 cm^{-1}, which correspond to the characteristic D band and G band, respectively. Note that the D-band intensity (I_D) is stronger than the G-band intensity (I_G), indicating the abundant defects and edges in the CTF-Super P catalysts.

The morphology and microstructure of the CTF-Super P catalysts are investigated by scanning electron microscopy (SEM) and transmission electron microscopy (TEM). As shown in Fig. 2a, the CTF itself shows a layered bulk structure with a size of dozens of microns, and Super P comprises plenty of relatively regular spherical particles with a size of 40–50 nm (Fig. S1a, b, e and f†). When Super P was added to the CTF precursors, however, the morphology changes obviously. Many sheet-like structures can be readily observed, and the aggregation of spherical particles (Super P) was found on the surface of the nanosheets (Fig. 2b). In concert with the SEM results, the typical TEM images of CTF and CTF-Super P-10 (a systematically studied sample with the best performance in the ORR) are shown in Fig. 2c and d and S1.† Intimate contact between the nanoparticles and nanosheets is revealed by high-resolution TEM (Fig. 2c), and abundant holes and potholes can be clearly seen by STEM (Fig. 2d).

To further explore the influence of Super P on the structure, the specific surface areas (SSAs) and pore size distributions of CTF, Super P and CTF-Super P composites had been examined by N_2 adsorption/desorption measurements. As shown in Fig. 3a, the CTF control displays the features of type I isotherms, owing to the presence of micropores, and Super P exhibits a type II isotherm. Note that CTF-Super P-5, CTF-Super P-10 and CTF-Super P-15 show type IV isotherms

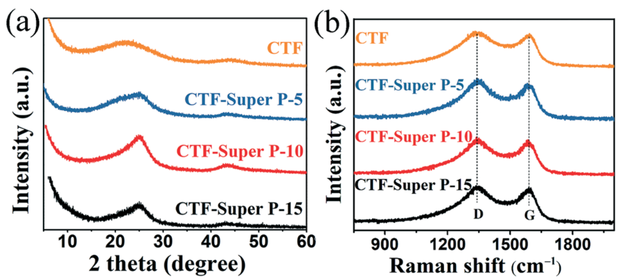

Fig. 1 (a) XRD patterns and (b) Raman spectra of CTF, CTF-Super P-5, CTF-Super P-10, and CTF-Super P-15.

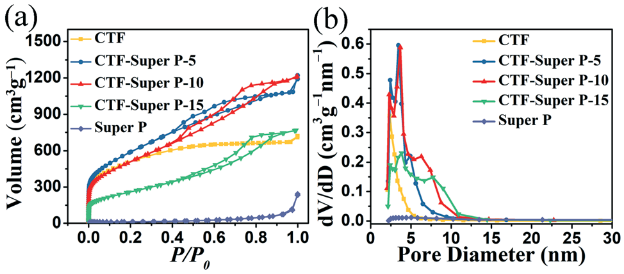

Fig. 3 (a) Nitrogen adsorption/desorption isotherms and (b) pore size distributions obtained by the BJH method of CTF, CTF-Super P-5, CTF-Super P-10, CTF-Super P-15 and Super P.

with H2(b) type hysteresis loops. The pore size distribution curves obtained by the Barrett–Joyner–Halenda (BJH) method confirm the presence of abundant mesopores with a pore size of 2–12 nm (Fig. 3b). Compared with the pure CTF, the SSAs of the CTF-Super P composites can be increased from 1680 to 1925 $m^2\ g^{-1}$ (Table S1†), attributed to the abundant holes and potholes observed by STEM above. The addition of Super P effectively avoids the aggregation of CTF blocks, and the increased exposed surface area and porosity result from the staking pores of nanoparticles and nanosheets. However, a further increase of the Super P content will also result in a sudden decrease of SSA, as the SSA of Super P here is only 49 $m^2\ g^{-1}$, which is far lower than the SSA of its CTF counterpart. In general, hierarchical micro/mesoporous structures and high BET surface areas could provide more edges and defects,[10] which not only expose more catalytic active sites for the ORR, but also enhance the electron transfer and oxygen diffusion.[35,36]

The compositions and the surface chemical states of CTF and CTF-Super P-10 are evaluated by X-ray photoelectron spectroscopy (XPS) (Fig. 4 and Table S2†). The high resolution N1s spectra reveal the presence of four nitrogen species: pyridinic N (~398.3 eV), pyrrolic N (~399.5 eV), graphitic N (~401.0 eV) and oxidized N (~404.1 eV).[37] Quantitative analysis shows that CTF-Super P-10 has much more pyridinic N and graphitic N and less pyrrolic N, when compared with the CTF. In particular, the content of pyridinic N on the material surface increases significantly. Based on this result, it is proposed that the addition of Super P affects the transformation process of various nitrogen species in CTF building blocks, although the mechanism involved remains unclear. Previous studies have confirmed that pyridinic N and graphitic N are active towards the ORR, which can improve the onset potential and the limiting current density.[9,37–41] Given the high content of pyridinic N and graphitic N in CTF-Super P-10, excellent ORR activity was expected.

This assumption was confirmed by the rotating disk electrode (RDE) experiments that were carried out with a standard three-electrode system. As shown in Fig. 5a, the LSV curves of the samples were obtained in an O_2-saturated 0.1 M KOH electrolyte at a rotating speed of 1600 rpm with a Pt counter electrode. The onset potential (E_o, measured at a current density of 0.1 mA cm^{-2}), half-wave potential ($E_{1/2}$) and limiting current density (J_m, measured at a potential of 0.2 V *vs.* RHE) are summarized in Table S3.† It can be seen that the addition of Super P to the CTF precursors could significantly affect the ORR performance. With the increase of Super P content, the ORR activity increases at first and then decreases. Specifically, CTF-Super P-10 exhibits the best ORR activity, with an onset potential of 0.981 V, a half-wave potential of 0.883 V, and the highest limiting current density of 5.31 mA cm^{-2}, compared to pure CTF (E_o = 1.01 V, $E_{1/2}$ = 0.881 V, J_m = 4.76 mA cm^{-2}). However, a further increase of the Super P content will result in inferior ORR activity. A negative onset potential of 0.949 V, a half-wave potential of 0.838 V, and a low limiting current density of 4.55 mA cm^{-2} were obtained for CTF-Super P-15.

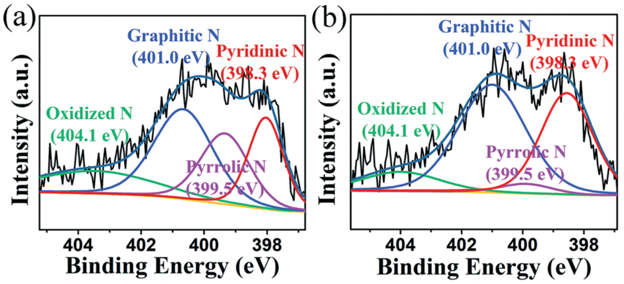

Fig. 4 XPS N1s deconvolution results of (a) CTF and (b) CTF-Super P-10.

The poisoning experiments were performed by adding 1 mM KSCN to identify the active species in CTF-Super P-10 (Fig. S2†). The LSV curves showed little change before and after the addition of the toxicant, suggesting that the excellent ORR activities of CTF-Super P-10 should come from the nonmetallic active sites. The electrical impedance spectroscopy (EIS) tests were also conducted to evaluate the electron transfer resistance (Fig. S3†). The Nyquist plots demonstrate that CTF-Super P-10 exhibits a smaller semicircle diameter than CTF. The R_{ct} of CTF-Super P-10 is calculated to be 12.4 Ω, obviously smaller than that of CTF (17.5 Ω), indicating its lower charge transfer resistance and better electrical conductivity.

Combined with the results above, the excellent electrochemical performance of CTF-Super P-10 should be explained by its improved conductivity, large specific surface area (1925 $m^2\ g^{-1}$), desirable hierarchical micro/mesoporous structure and abundant pyridinic N and graphitic N content. In particular, the hierarchical structure not only increases the number of catalytic active sites and exposes more active sites, but also facilitates the mass transfer process of electrolyte during the ORR. Note that the performance of the CTF-Super P-10 here is comparable to the commercial Pt/C electrodes, as well as state-of-the-art N-doped carbon-based ORR catalysts (Tables S3 and S4†).

To determine the selectivity of CTF-Super P-10 during the ORR process, LSV curves at different rotating rates (Fig. 5b) and the corresponding Koutecky–Levich (K–L) plots (Fig. 5c) were collected. The calculated electron transfer number is 3.67, indicating that a four-electron pathway dominates the ORR process in the alkaline electrolyte. The results were further evaluated by rotating ring-disk electrode (RRDE) measurements (Fig. 5d). The HO_2^- yield in 0.1 M KOH solution remains below 6% over the potential range of 0.20 V to 0.80 V, corresponding to a high electron transfer number ranging from 4.01 to 4.13, which is close to the K–L plots.

Besides their excellent catalytic activity, the stability and poison tolerance of the catalysts were also tested. As shown in Fig. 5e, after the addition of 3 M methanol, no response was observed for CTF-Super P-10, while the current density dropped quickly when using Pt/C as the ORR catalyst. Note that CTF-Super P-10 also displays strong stability under alkaline conditions (Fig. 5f), which overcomes another disadvantage faced by the Pt/C catalyst. After 5000 potential cycles of

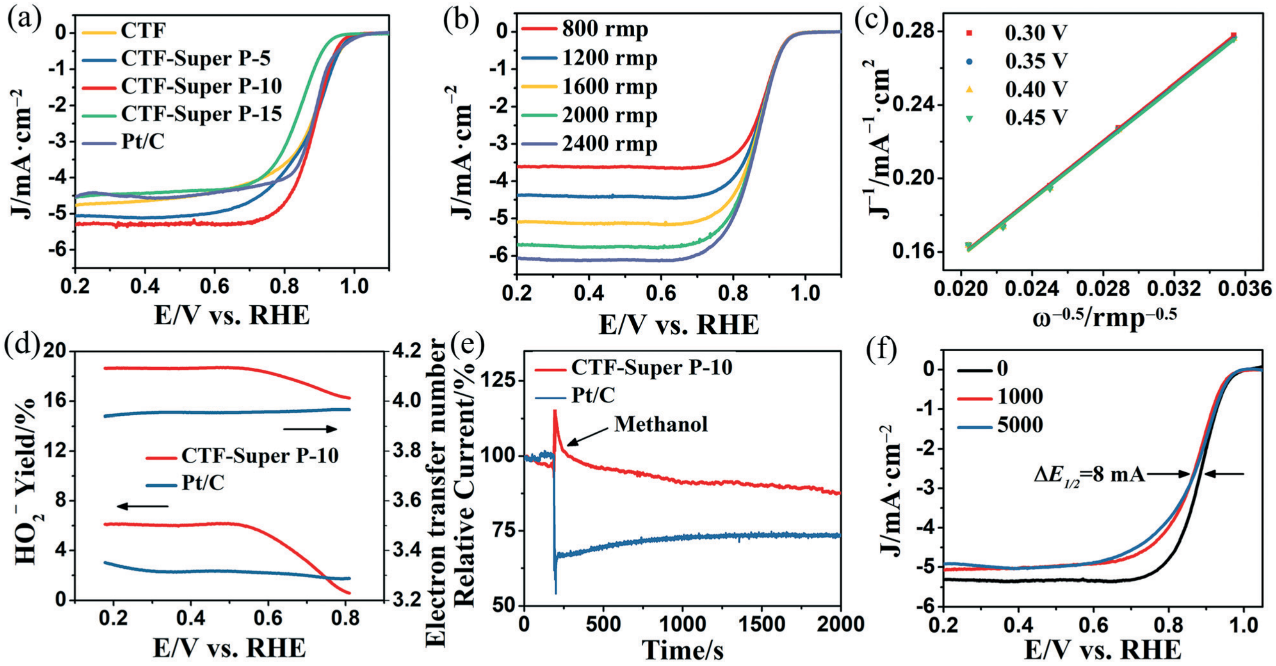

Fig. 5 (a) LSV curves of CTF, CTF-Super P-5, CTF-Super P-10, CTF-Super P-15, and Pt/C at a rotation rate of 1600 rpm with a scan rate of 10 mV s^{-1} in O_2-saturated 0.1 M KOH solution. (b) LSV curves of CTF-Super P-10 at different RDE rotation rates and (c) K–L plots at various potentials. (d) HO_2^- yields and electron transfer numbers of CTF-Super P-10 and Pt/C. (e) Methanol tolerance curves of CTF-Super P-10 and Pt/C. (f) LSV results of CTF-Super P-10 before and after 5000 potential cycles. The above data were tested with a Pt counter electrode.

the accelerated durability test, the $E_{1/2}$ of CTF-Super P-10 only dropped by 8 mA. The comparison results clearly demonstrate the better poison tolerance and strong stability of the CTF-Super P-10 catalyst under alkaline conditions. The activity and stability of the samples were also investigated with a carbon counter electrode to rule out the possibility of the influence of the counter electrode (Fig. S4 and Table S5†).[1] The results showed that the performance using carbon as the

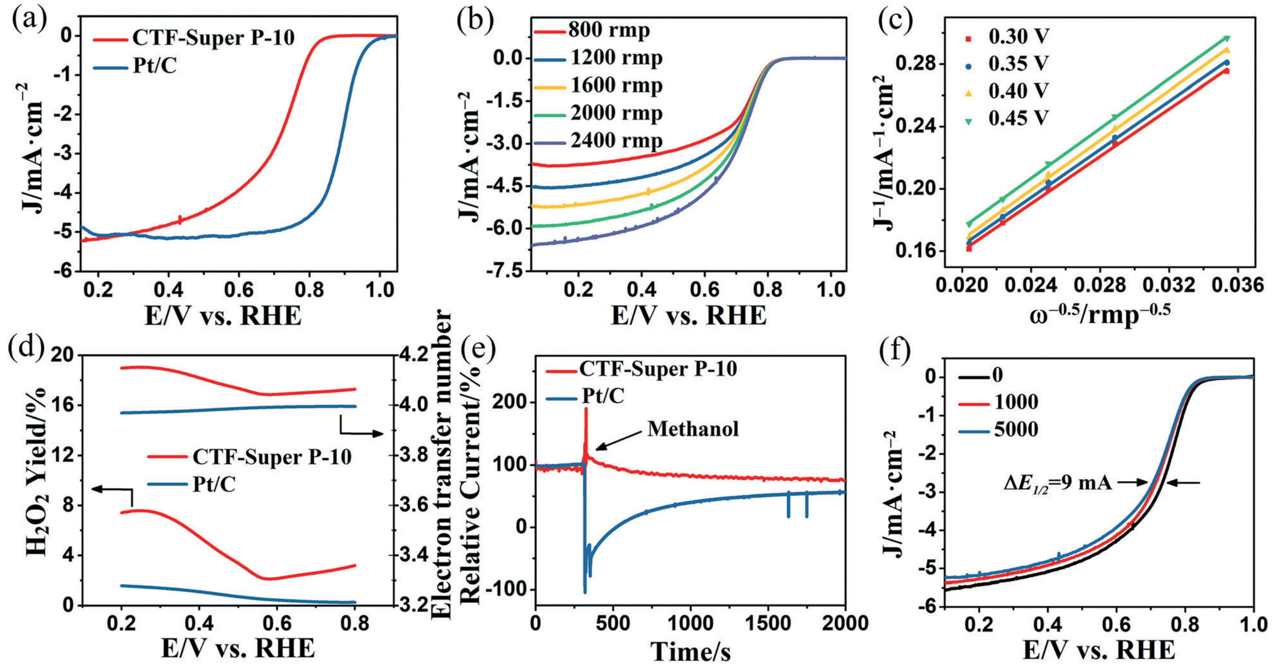

Fig. 6 (a) LSV curves of CTF-Super P-10 and Pt/C at a rotation rate of 1600 rpm with a scan rate of 10 mV s^{-1} in O_2-saturated 0.1 M $HClO_4$ solution. (b) LSV curves of CTF-Super P-10 at different RDE rotation rates and (c) K–L plots at various potentials. (d) H_2O_2 yields and electron transfer numbers of CTF-Super P-10 and Pt/C. (e) Methanol tolerance curves of CTF-Super P-10 and Pt/C. (f) LSV results of CTF-Super P-10 before and after 5000 potential cycles. The above data were tested with a Pt counter electrode.

counter electrode is almost identical with that using Pt as the counter electrode.

The excellent ORR activity of CTF-Super P-10 under alkaline conditions prompted us to investigate its performance in acidic media. The LSV curves in Fig. 6 and S4c and d† were obtained in an O_2-saturated 0.1 M $HClO_4$ electrolyte. CTF-Super P-10 displays an onset potential of 0.840 V and a half-wave potential of 0.717 V, with a limiting current density of 5.40 mA cm^{-2} with a Pt counter electrode (E_o = 0.847 V, $E_{1/2}$ = 0.734 V, J_m = 5.45 mA cm^{-2} with a carbon counter electrode). Although the behavior of CTF-Super P-10 is inferior to that of Pt/C in acidic medium, it is better than those of most reported metal-free catalysts (Table S4†). Its unideal activity may be due to the protonation of the surface N-groups under acidic conditions, which is consistent with most reports on N-doped carbon materials.[5] Similar to the results under alkaline conditions, CTF-Super P-10 shows low H_2O_2 yield and a four-electron pathway in the ORR process based on the K–L plots and RRDE technique. In Fig. S3b,† the lower electron transfer impedance of CTF-Super P-10 suggests its superior electron transfer ability during the ORR, and the LSV curves completely coincide before and after the addition of the toxicant. Furthermore, CTF-Super P-10 is highly durable and has better methanol tolerance than Pt/C.

Conclusions

In summary, following an ionothermal synthesis and pyrolysis process, N-doped hierarchical porous carbon materials were prepared by regulating the proportion of Super P in the aromatic nitrile precursors. Owing to its hierarchical micro/mesoporous structure, high specific surface area, enhanced conductivity and high content of pyridine N and graphitic N, CTF-Super P-10 shows excellent ORR performance in both alkaline solution and acidic solution. It was found that the overall catalytic performance of CTF-Super P-10 surpassed those of most reported metal-free catalysts and even that of commercial Pt/C. The strategy here may be also applicable in preparing other hierarchical heteroatom-doped carbon based catalysts for energy storage and conversion.

Conflicts of interest

There are no conflicts to declare.

Acknowledgements

This study is supported by the National Natural Science Funds (No. 21878226).

Notes and references

1 A. A. Gewirth, J. A. Varnell and A. M. DiAscro, *Chem. Rev.*, 2018, **118**, 2313–2339.

2 P. Peng, Z. Zhou, J. Guo and Z. Xiang, *ACS Energy Lett.*, 2017, **2**, 1308–1314.

3 C. Zhang, S. Y. Hwang, A. Trout and Z. Peng, *J. Am. Chem. Soc.*, 2014, **136**, 7805–7808.

4 R. Silva, D. Voiry, M. Chhowalla and T. Asefa, *J. Am. Chem. Soc.*, 2013, **135**, 7823–7826.

5 L. Jiao, Y. Hu, H. Ju, C. Wang, M.-R. Gao, Q. Yang, J. Zhu, S.-H. Yu and H.-L. Jiang, *J. Mater. Chem. A*, 2017, **5**, 23170–23178.

6 C. Y. Lin, D. Zhang, Z. Zhao and Z. Xia, *Adv. Mater.*, 2018, **30**, 1703646.

7 L. Dai, Y. Xue, L. Qu, H. J. Choi and J. B. Baek, *Chem. Rev.*, 2015, **115**, 4823–4892.

8 Y. Xu, S. Jin, H. Xu, A. Nagai and D. Jiang, *Chem. Soc. Rev.*, 2013, **42**, 8012–8031.

9 L. Li, P. Dai, X. Gu, Y. Wang, L. Yan and X. Zhao, *J. Mater. Chem. A*, 2017, **5**, 789–795.

10 C. Tang, B. Wang, H. F. Wang and Q. Zhang, *Adv. Mater.*, 2017, **29**, 1703185.

11 C. Zhu, H. Li, S. Fu, D. Du and Y. Lin, *Chem. Soc. Rev.*, 2016, **45**, 517–531.

12 J. Wu, F. Xu, S. Li, P. Ma, X. Zhang, Q. Liu, R. Fu and D. Wu, *Adv. Mater.*, 2019, **31**, e1802922.

13 F. Kong, Y. Qiao, C. Zhang, R. Li, T. Cheng, A. Kong and Y. Shan, *Catal. Sci. Technol.*, 2019, **9**, 3469–3481.

14 T.-N. Tran, C.-H. Shin, B.-J. Lee, J. S. Samdani, J.-D. Park, T.-H. Kang and J.-S. Yu, *Catal. Sci. Technol.*, 2018, **8**, 5368–5381.

15 Y. Li, Y. Zhou, C. Zhu, Y. H. Hu, S. Gao, Q. Liu, X. Cheng, L. Zhang, J. Yang and Y. Lin, *Catal. Sci. Technol.*, 2018, **8**, 5325–5333.

16 P. Kuhn, M. Antonietti and A. Thomas, *Angew. Chem., Int. Ed.*, 2008, **47**, 3450–3453.

17 C. S. Diercks and O. M. Yaghi, *Science*, 2017, **355**, eaal1585.

18 K. Gong, F. Du, Z. Xia, M. Durstock and L. Dai, *Science*, 2009, **323**, 760.

19 L. Qu, Y. Liu, J.-B. Baek and L. Dai, *ACS Nano*, 2010, **4**, 1321–1326.

20 J. Shui, M. Wang, F. Du and L. Dai, *Sci. Adv.*, 2015, **1**, e1400129.

21 J. Zhang, Z. Zhao, Z. Xia and L. Dai, *Nat. Nanotechnol.*, 2015, **10**, 444–452.

22 D. Guo, R. Shibuya, C. Akiba, S. Saji, T. Kondo and J. Nakamura, *Science*, 2016, **351**, 361.

23 X. Deng, B. Zhao, L. Zhu and Z. Shao, *Carbon*, 2015, **93**, 48–58.

24 P. Kuhn, A. Forget, D. Su, A. Thomas and M. Antonietti, *J. Am. Chem. Soc.*, 2008, **130**, 13333–13337.

25 O. Buyukcakir, S. H. Je, S. N. Talapaneni, D. Kim and A. Coskun, *ACS Appl. Mater. Interfaces*, 2017, **9**, 7209–7216.

26 L. Hao, S. Zhang, R. Liu, J. Ning, G. Zhang and L. Zhi, *Adv. Mater.*, 2015, **27**, 3190–3195.

27 Y. Zhu, X. Chen, J. Liu, J. Zhang, D. Xu, W. Peng, Y. Li, G. Zhang, F. Zhang and X. Fan, *ChemSusChem*, 2018, **11**, 2402–2409.

28 D. G. Wang, H. Wang, Y. Lin, G. Yu, M. Song, W. Zhong and G. C. Kuang, *ChemSusChem*, 2018, **11**, 3932–3940.

29 U. Stoeck, J. Balach, M. Klose, D. Wadewitz, E. Ahrens, J. Eckert and L. Giebeler, *J. Power Sources*, 2016, **309**, 76–81.

30 H. Liao, H. Ding, B. Li, X. Ai and C. Wang, *J. Mater. Chem. A*, 2014, **2**, 8854–8858.

31 S. H. Je, H. J. Kim, J. Kim, J. W. Choi and A. Coskun, *Adv. Funct. Mater.*, 2017, **27**, 1703947.

32 K. Kamiya, R. Kamai, K. Hashimoto and S. Nakanishi, *Nat. Commun.*, 2014, **5**, 5040.

33 K. Iwase, T. Yoshioka, S. Nakanishi, K. Hashimoto and K. Kamiya, *Angew. Chem., Int. Ed.*, 2015, **54**, 11068–11072.

34 P. Su, K. Iwase, T. Harada, K. Kamiya and S. Nakanishi, *Chem. Sci.*, 2018, **9**, 3941–3947.

35 J. Liu, Y. Liu, D. Xu, Y. Zhu, W. Peng, Y. Li, F. Zhang and X. Fan, *Appl. Catal., B*, 2019, **241**, 89–94.

36 X. Hua, J. Luo, C. Shen and S. Chen, *Catal. Sci. Technol.*, 2018, **8**, 1945–1952.

37 Z. Song, W. Liu, N. Cheng, M. Norouzi Banis, X. Li, Q. Sun, B. Xiao, Y. Liu, A. Lushington, R. Li, L. Liu and X. Sun, *Mater. Horiz.*, 2017, **4**, 900–907.

38 X. Lin, P. Peng, J. Guo and Z. Xiang, *Chem. Eng. J.*, 2019, **358**, 427–434.

39 M. Yang, X. Long, H. Li, H. Chen and P. Liu, *ACS Sustainable Chem. Eng.*, 2018, **7**, 2236–2244.

40 X. R. Wang, J. Y. Liu, Z. W. Liu, W. C. Wang, J. Luo, X. P. Han, X. W. Du, S. Z. Qiao and J. Yang, *Adv. Mater.*, 2018, **30**, e1800005.

41 X. Huang, X. Wu, Y. Niu, C. Dai, M. Xu and W. Hu, *Catal. Sci. Technol.*, 2019, **9**, 711–717.